Nonlinear Dyn (2016) 85:2467–2486
DOI 10.1007/s11071-016-2838-6

ORIGINAL PAPER

Nonlinear vibrations of a flexible membrane under periodic load

Xu Sun · Jia-zhong Zhang

Received: 4 July 2015 / Accepted: 6 May 2016 / Published online: 4 June 2016
© Springer Science+Business Media Dordrecht 2016

Abstract A finite element solution procedure is proposed, and the nonlinear vibrations of a flexible membrane under periodic load are investigated numerically. First, a simplified model is proposed for the flow-induced vibration of a membrane wing at higher angles of attack and the corresponding governing equation is derived briefly. Then, a solution procedure based on the Galerkin finite element method, Generalized-α method and Newton–Raphson method is developed to solve the governing equation and its accuracy and stability are examined by a steady problem with exact solution. Finally, using the numerical method proposed, the forced vibration of a flexible membrane under periodic load is simulated, and the effects of the membrane density, elastic modulus and pre-strain are investigated in detail. In addition, the change in the vibration state along the membrane is also analysed to examine whether the centre point can reflect correctly the vibration state of the whole structure.

Keywords Finite element method · Forced vibration · Flexible membrane · Periodic load · Nonlinear vibration

X. Sun (✉)
National Engineering Laboratory for Pipeline Safety/MOE Key Laboratory of Petroleum Engineering, China University of Petroleum-Beijing, Beijing, China
e-mail: xsun@cup.edu.cn

J. Zhang
School of Energy and Power Engineering, Xi'an Jiaotong University, Xi'an 710049, China

1 Introduction

In nature and engineering, there are various types of membrane structures such as heart valves, parachutes, sails, wings of micro-aerial vehicles (MAVs) and flying insects, and lightweight fabric building structures. Usually, these structures are very flexible and easy to deform or vibrate even when the velocity of the surrounding flow is very small. For the membrane structures such as parachutes, sails and lightweight fabric building structures, the flow-induced deformation (FID) and flow-induced vibration (FIV) are usually harmful and may lead to instability, fatigue failure or even breakage of the structure. For MAVs and flying insects, however, FID and FIV of the membrane wing could enhance significantly their aerodynamic performance. Hence, the fluid–membrane interaction (FMI) problem has attracted a lot of attention in the past a few decades.

The study of FMI could be traced back to the 1980s in the background of sail design. In the earlier studies, FID of the sail under external flow was mainly concerned. In 1986, using the potential flow model and supposing the membrane as a weightless chain of thin tracts, de Matteis and de Socio [1] studied the FID of a two-dimensional (2D) membrane at different angles of attack (AOAs). In their research, the computed membrane deformation agreed very well with the experimental results at smaller AOAs but had a large discrepancy at higher AOAs, due to the poor performance of the potential flow model when large-scale separa-

tion appears in the flow. In 1994, to better describe the flow separation, Rast [2] proposed an improved FMI model by combining the steady Navier–Stokes (NS) equations and a steady membrane equation considering both normal and tangential flow stresses, and the FID of a piece of membrane wall in a 2D channel with laminar internal flows ($Re = 10-300$) was simulated to study the nature of partial collapses of elastic tubes conveying fluid in physiological settings such as blood vessels and large airways.

In the 1990s, FIV of the membrane structures began to receive attention. In 1995, by combining the unsteady NS equations and a steady membrane equation, Smith and Shyy [3] investigated the unsteady response of a membrane wing in the laminar flow ($Re = 4000$) with a periodic free-stream velocity. In 1996, this FMI model was modified and extended to the case with turbulent flow by taking the unsteady Reynolds-averaged NS (RANS) equations and shear stress transport (SST) $k - \omega$ turbulence model as the governing equations of the flow field [4]. In both studies of [3,4], the aerodynamic performances of the membrane wing at higher AOAs were predicted more accurately than those obtained from the FMI model ignoring the fluid viscosity [1]. However, since a steady equation was employed to describe FIV of the membrane wing, the FMI model proposed by Smith and Shyy [3,4] was still quasi-unsteady.

Subsequently, the FMI model proposed by Smith and Shyy [3,4] was further improved by other researchers to capture the dynamic response of the membrane structure in viscous flows. In 1997, Liang et al. [5] proposed a deformable spatial domain space–time algorithm for FMI problems. Different from the model of Smith and Shyy [3,4], the FMI model in [5] took the effects of inertia/mass into account, and the FIV of a lid driven cavity with flexible bottom was simulated successfully. In 2008, combing the unsteady incompressible NS equations with a structure model taking the membrane as a chain of nodes connected by a spring and dashpot system, Matthews et al. [6] computed the dynamic response of a 2D membrane wing in a laminar flow with $Re = 4000$. Different from the steady models in [1,2] and quasi-unsteady models in [3,4], the FMI models in [5,6] are unsteady and capable of capturing the dynamic response of the membrane structures in unsteady flows with large-scale separation and vortex shedding. However, in the works of Liang et al. [5] and Matthews et al. [6], the fluid–structure interaction (FSI) algorithm was mainly concerned, while the dynamic behaviours of the membrane under time-varying fluid loads were not discussed in detail.

Recently, with rapid development of MAVs, more studies [7–12] have been carried out on the FIV of the fixed membrane wing. From 2009 to 2011, Rojratsirikul et al. [7–9] conducted many experiments on the FMI of the membrane wing and found that FIV of the membrane could promote reattachment of the separated shear layer, delay stall and increase significantly the lift of the membrane wing at higher AOAs. Subsequently, these findings were confirmed by Gordnier et al. [10–12] using numerical simulation. In [10–12], taking the unsteady compressible NS equations and an unsteady membrane equation as the governing equations and using a strongly coupled algorithm for FSI simulation, FMIs of the membrane wing in flows with lower Reynolds numbers ($Re = 2500$, 5000 and 10,000) were successfully simulated, and the effects of AOA, rigidity, pre-strain and Reynolds number on the aerodynamic performance as well as the dynamic response of the membrane wing were analysed. Based on the numerical results, it was found that, for a fixed membrane wing, not only the amplitude and dominant frequency but also the state of FIV of the membrane wing will change with the flow and structure parameters. Subsequently, this FSI solver was improved and utilized by Jaworski and Gordnier [13,14], Visbal et al. [15] and Tregidgo et al. [16] to study the dynamic responses of the membrane wing with prescribed pitching and/or heaving motions, and it was found that the FMIs could decrease the separation region, enhance thrust and propulsive efficiency and increase the adaptability of the membrane wing to the transient gust. In addition, Arbós-Torrent [17] observed from their experiments that the shape of the leading and trailing edges has a great effects on the FIV of the membrane wing; Curet et al. [18] found that coupling the forced harmonic oscillation with the FIV could increase significantly the lift of the membrane wing; Serrano-Galiano and Sandberg [19] proposed a direct numerical simulation (DNS) method for the FMI with transition in the flow field; Bleischwitz et al. [20] investigated the aspect-ratio effect on the aerodynamic performance of the membrane wing and found that decreasing the aspect ratio could suppress stall and increase the pitching stability; Bleischwitz et al. [21] revealed that the ground effect could result in an earlier onset of the

leading-edge vortex shedding and excite highly energetic oscillation of the membrane wing.

In the numerical studies of Gordnier et al. [10–12], the unsteady flow as well as the FIV state of the membrane wing was found changed greatly with the angle of attack, Reynolds number, rigidity and pre-strain of the membrane. However, because FSI simulation has to solve both flow and structure domains and is very time-consuming, only 3 or 5 values of each parameter were considered in these studies [10–12], and a thorough simulation of the bifurcation process of the FIV of the membrane wing with respect to each parameter, which usually needs to compute hundreds or even thousands of points for each parameter, has not been done yet.

In this paper, a simplified FMI model is proposed to reveal the bifurcation characteristics of the dynamic response of a membrane wing under periodic aerodynamic loads at higher AOAs, and the effects of the structure parameters including the membrane density, elastic modulus and pre-strain are analysed in detail. In addition, bifurcation of the vibration state along the membrane is also discussed to examine whether the centre point, which is usually taken as the monitor point in many previous studies [7–12], can reflect correctly the vibration state of the whole membrane. This paper might help people get a better understanding of the FIV of the membrane structures in the flow with large-scale separation.

2 FMI model

In Fig. 1, a membrane wing model is proposed based on the experimental model of Rojratsirikul et al. [7–9], which is formed by gluing a thin latex sheet to the rigid mounts at both leading and trailing edges. As shown in this figure, when there is flow past the membrane wing, the membrane will deform to the leeward side of the wing due to the pressure difference between the lower and upper surfaces. At very small AOAs, the membrane wing might eventually stay at a static equilibrium position after a transient process. At higher AOAs, however, since the fluid load becomes unsteady due to separation and vortex shedding on the upper surface, the membrane wing cannot stay at a static equilibrium position but will vibrate with time. To describe the deformation of a membrane wing under fluid load, a local coordinate system is established in Fig. 1. In this local coordinate system, the leading edge is taken as the origin of coordinates, the x axis is along the wing chord, and the z axis is perpendicular to the wing chord and directed to the leeward side. Consider the dynamic equilibrium of an elementary length $\mathrm{d}l$ of the membrane wing. In principle, the lower and upper surfaces of this element are subjected to both normal and shear stresses from the fluid and it will deform in both x and z directions. However, considering the deformation of the membrane is mainly driven by the pressure difference between the lower and upper surfaces, the shear stress and other components of the normal stress except for the pressure are ignored and the deformation is supposed to be only in z direction. In addition, since the thickness of the membrane is very small, shear forces and bending moments at the two ends and the gravity of the membrane element are also ignored.

Based on the assumptions stated above, the external loads imposed on the membrane element are presented in Fig. 1. As shown in the figure, the pressures on the upper and lower surfaces are p^+ and p^-, respectively, the membrane element is subjected to the same tension T at both ends, and the damping force per unit length is f_D, the direction of which is always opposite to the motion. Following Newton's second law, vibration equation of this membrane element can be expressed by

$$\rho_S h \mathrm{d}l \frac{\partial^2 z}{\partial t^2} = \left(p^- - p^+\right) \mathrm{d}l + T \sin(\theta + \mathrm{d}\theta) - T \sin\theta - f_D \mathrm{d}l \quad (1)$$

where ρ_S is the membrane density, h the thickness, z the displacement and θ the angle between the tension and horizontal line in Fig. 1. Suppose that the lateral deformation z is not large and both θ and $\mathrm{d}\theta$ are small values. Then, substituting $\sin\theta \approx \theta$, $\sin(\theta + \mathrm{d}\theta) \approx \theta + \mathrm{d}\theta$ and also $f_D = \rho_S C_d \frac{\partial z}{\partial t}$ into Eq. (1) yields

$$\rho_S h \frac{\partial^2 z}{\partial t^2} + \rho_S C_d \frac{\partial z}{\partial t} - T \frac{\mathrm{d}\theta}{\mathrm{d}l} = p^- - p^+ \quad (2)$$

where $\mathrm{d}\theta/\mathrm{d}l$ is the curvature and can be computed by

$$\frac{\mathrm{d}\theta}{\mathrm{d}l} = \frac{\partial^2 z}{\partial x^2} \left[1 + \left(\frac{\partial z}{\partial x}\right)^2\right]^{-\frac{3}{2}} \quad (3)$$

Assume the membrane material is linearly elastic and therefore the membrane tension can be further expressed as

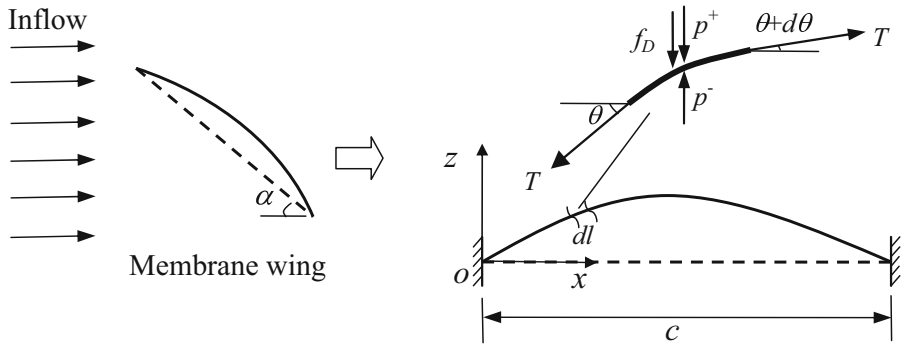

Fig. 1 A mechanical model of a membrane wing under fluid load

$$T = Eh\left(\delta_0 + \bar{\delta}\right) \tag{4}$$

where E is the elastic modulus, δ_0 the pre-strain and $\bar{\delta}$ the strain, which can be calculated by

$$\bar{\delta} = \frac{L_S - L_0}{L_0} \tag{5}$$

In Eq. (5), L_0 and L_S are the membrane lengths before and after deformation, respectively, and L_S can be computed by

$$L_S = \int_0^c \sqrt{1 + \left(\frac{\partial z}{\partial x}\right)^2}\,\mathrm{d}x \tag{6}$$

In Eq. (2), $p^- - p^+ = \Delta p$ is the fluid load imposed on the membrane wing. For FSI problems, this term is determined not only by the flow parameters such as the Reynolds number and AOA (α in Fig. 1) but also affected by the structure parameters such as ρ_S, h, C_d, E and δ_0. Hence, Δp could be expressed generally by $\Delta p = Q(Re,\ \alpha,\ \rho_S,\ h,\ C_d,\ E,\ \delta_0,\ x, t)$. As mentioned above, when AOA is very small, the membrane wing might eventually stay at a static equilibrium position and be subjected to a steady fluid load. In this case, the relationship between Δp and the flow and structure parameters can be simplified to $\Delta p = Q'(Re,\ \alpha,\ h,\ E,\ \delta_0, x)$. In the work of Waldman and Breuer [22], a specific form of Q' is proposed for the case at small AOAs by assuming that Δp is uniform over the membrane wing and the lift is equal to the circular arcs in potential flow. Unfortunately, to the best of our knowledge, the specific form of Q has not been reported yet for the case at higher AOAs due to the complexity of the relationship. In this paper, to investigate the dynamic response of a membrane wing under periodic fluid load at higher AOAs, a simple form of Q is proposed by supposing Δp is periodic and distributed uniformly over the membrane, namely

$$\Delta p = \sigma \sin(2\pi f_e t) \tag{7}$$

where σ is the amplitude and f_e the oscillating frequency. Substituting Eqs. (3) and (7) into Eq. (2), the vibration equation of a membrane wing under periodic fluid load can be derived as

$$\rho_S h \frac{\partial^2 z}{\partial t^2} + \rho_S C_d \frac{\partial z}{\partial t} - T\frac{\partial^2 z}{\partial x^2}\left[1 + \left(\frac{\partial z}{\partial x}\right)^2\right]^{-\frac{3}{2}} = \sigma \sin(2\pi f_e t) \tag{8}$$

Furthermore, take U, $L = c$ and ρ_0 as the reference velocity, length and density, respectively, and define

$$\begin{aligned}
&\tilde{x} = x/L, \quad \tilde{t} = tU/L, \quad \tilde{C}_d = C_d/U,\\
&\qquad \tilde{\rho}_S = \rho_S/\rho_0, \quad \tilde{h} = h/L,\\
&\tilde{c} = c/L = 1.0, \quad \tilde{f}_e = f_e L/U, \quad \tilde{z} = z/L,\\
&\qquad \tilde{L}_S = L_S/L, \quad \tilde{L}_0 = L_0/L,\\
&E = E/\left(\rho_0 U^2\right), \quad \tilde{\sigma} = \sigma/\left(\rho_0 U^2\right),\\
&\qquad \tilde{T} = TL/\left(\rho_0 U^2\right).
\end{aligned} \tag{9}$$

The non-dimensional form of the governing equations can be obtained as

$$\begin{cases}
\tilde{\rho}_S \tilde{h}\dfrac{\partial^2 \tilde{z}}{\partial \tilde{t}^2} + \tilde{\rho}_S \tilde{C}_d \dfrac{\partial \tilde{z}}{\partial \tilde{t}} - \tilde{T}\dfrac{\partial^2 \tilde{z}}{\partial \tilde{x}^2}\left[1 + \left(\dfrac{\partial \tilde{z}}{\partial \tilde{x}}\right)^2\right]^{-\frac{3}{2}} \\
\quad = \tilde{\sigma}\sin(2\pi \tilde{f}_e \tilde{t}),\\
\tilde{T} = \tilde{E}\tilde{h}\left(\delta_0 + \bar{\delta}\right), \bar{\delta} = \dfrac{\tilde{L}_S - \tilde{L}_0}{\tilde{L}_0}, \tilde{L}_S \\
\quad = \int_0^{\tilde{c}=1} \sqrt{1 + \left(\frac{\partial \tilde{z}}{\partial \tilde{x}}\right)^2}\,\mathrm{d}\tilde{x}.
\end{cases} \tag{10}$$

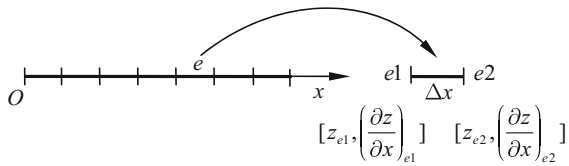

Fig. 2 A schematic of the membrane elements

In the rest of this paper, the non-dimensional symbol "∼" in Eqs. (9) and (10) is dropped for convenience.

3 Numerical method

3.1 Spatial discretization

As shown in Fig. 2, the membrane is first divided into M parts with the same length of Δx, and then the Hermite polynomial is used to approach the deformation of each element using the displacements and gradients at the two end nodes, namely

$$z_e(x) = N_{e1} z_{e1} + N_{e2}\left(\frac{\partial z}{\partial x}\right)_{e1} + N_{e3} z_{e2} + N_{e4}\left(\frac{\partial z}{\partial x}\right)_{e2}, \tag{11}$$

where $e1$ and $e2$ denote the left and right end nodes of element e, respectively, and the interpolation functions in element e can be expressed by

$$N_{e1} = 1 - 3\xi^2 + 2\xi^3, \quad N_{e2} = \Delta x(\xi - 2\xi^2 + \xi^3),$$
$$N_{e3} = 3\xi^2 - 2\xi^3, \quad N_{e4} = \Delta x(\xi^3 - 2\xi^2), \tag{12}$$

where ξ is the local coordinate and defined by

$$\xi = (x - x_{e1})/(x_{e2} - x_{e1}). \tag{13}$$

Based on the approximate displacement on each element, the displacement $z(x)$ on the whole membrane can be expressed by

$$z(x) = N_1 z_1 + N_2\left(\frac{\partial z}{\partial x}\right)_1 \cdots + N_{(2I-1)} z_I + N_{2I}\left(\frac{\partial z}{\partial x}\right)_I \cdots + N_{(2M+1)} z_{(M+1)} + N_{2(M+1)}\left(\frac{\partial z}{\partial x}\right)_{(M+1)}, \tag{14}$$

where $N_{(2I-1)}$ and N_{2I} represent the shape functions of grid node I. Equation (14) can also be rewritten in the vector form as

$$z(x) = \mathbf{N} \cdot \mathbf{x} \tag{15}$$

where

$$\mathbf{N} = \{N_1, N_2, N_3 \cdots N_{2(M+1)}\},$$
$$\mathbf{x} = \left\{z_1, \left(\frac{\partial z}{\partial x}\right)_1, z_2, \left(\frac{\partial z}{\partial x}\right)_2 \cdots z_{(M+1)}, \left(\frac{\partial z}{\partial x}\right)_{(M+1)}\right\}^{\mathrm{T}}. \tag{16}$$

Substituting Eq. (16) into Eq. (10) and taking $\mathbf{N}$ as the weighting function yield

$$\mathbf{M}\ddot{\mathbf{x}} + \mathbf{C}\dot{\mathbf{x}} + \mathbf{K}(\mathbf{x})\mathbf{x} = \mathbf{Q} \tag{17}$$

where

$$\mathbf{M} = \rho_S h \int_0^1 \mathbf{N}^{\mathrm{T}}\mathbf{N}\mathrm{d}x \tag{18}$$

$$\mathbf{C} = \rho_S C_d \int_0^1 \mathbf{N}^{\mathrm{T}}\mathbf{N}\mathrm{d}x \tag{19}$$

$$\mathbf{K}(\mathbf{x}) = \int_0^1 \frac{\partial}{\partial x}\left\{\mathbf{N}^{\mathrm{T}} T\left[1 + \left(\frac{\partial \mathbf{N}\cdot\mathbf{x}}{\partial x}\right)^2\right]^{-\frac{3}{2}}\right\}\frac{\partial \mathbf{N}}{\partial x}\mathrm{d}x \tag{20}$$

$$\mathbf{Q} = \int_0^1 \mathbf{N}^{\mathrm{T}}\sigma \sin(2\pi f_e t)\mathrm{d}x \tag{21}$$

3.2 Time integration

It is obvious that Eq. (17) is a group of nonlinear ordinary partial differential equations, which can be integrated in time by algorithms such as the Runge–Kutta method, Newmark method or Generalized-α method. Considering its advantages in both accuracy and stability, the Generalized-α method proposed by Chung and Hulbert [23] is used here.

According to the Generalized-α method, Eq. (13) is further discretized in time as

$$\mathbf{M}\ddot{\mathbf{x}}_{n+1-\alpha_m} + \mathbf{C}\dot{\mathbf{x}}_{n+1-\alpha_f} + \mathbf{K}(\mathbf{x}_{n+1-\alpha_f})\mathbf{x}_{n+1-\alpha_f} = \mathbf{Q}(t_{n+1-\alpha_f}) \tag{22}$$

where

$$\begin{cases} \ddot{\mathbf{x}}_{n+1-\alpha_m} = (1-\alpha_m)\,\ddot{\mathbf{x}}_{n+1} + \alpha_m \ddot{\mathbf{x}}_n,\ \dot{\mathbf{x}}_{n+1-\alpha_f} \\ \quad = \left(1-\alpha_f\right)\dot{\mathbf{x}}_{n+1} + \alpha_f \dot{\mathbf{x}}_n, \\ \mathbf{x}_{n+1-\alpha_f} = \left(1-\alpha_f\right)\mathbf{x}_{n+1} + \alpha_f \mathbf{x}_n,\ t_{n+1-\alpha_f} \\ \quad = \left(1-\alpha_f\right) t_{n+1} + \alpha_f t_n, \\ \dot{\mathbf{x}}_{n+1} = \dot{\mathbf{x}}_n + \Delta t\left[(1-\gamma)\,\ddot{\mathbf{x}}_n + \gamma \ddot{\mathbf{x}}_{n+1}\right], \\ \quad \mathbf{x}_{n+1} = \mathbf{x}_n + \Delta t \dot{\mathbf{x}}_n + \Delta t^2\left[\left(\frac{1}{2}-\beta\right)\ddot{\mathbf{x}}_n + \beta \ddot{\mathbf{x}}_{n+1}\right], \\ \alpha_m = \dfrac{2\varsigma - 1}{\varsigma + 1},\ \beta = \dfrac{1}{4}\left(1-\alpha_m+\alpha_f\right)^2, \\ \quad \alpha_f = \frac{\varsigma}{\varsigma+1},\ \gamma = \frac{1}{2} - \alpha_m + \alpha_f, \end{cases} \tag{23}$$

In Eq. (23), $\varsigma \in [0, 1]$ is a governing parameter, which can control the high-frequency dissipation to vary from the no dissipation case ($\varsigma = 1$) to asymptotic annihilation case ($\varsigma = 0$). In this paper, $\varsigma = 0.1$ is used for all computations.

Substituting Eq. (23) into Eq. (22) and rearranging, a fully discretized form of Eq. (10) can be obtained as

$$\begin{aligned} &\left[\frac{1-\alpha_m}{\beta\Delta t^2}\mathbf{M} + \frac{\left(1-\alpha_f\right)\gamma}{\beta\Delta t}\mathbf{C}\right. \\ &\quad \left. + \left(1-\alpha_f\right)\mathbf{K}\left(\mathbf{x}_{n+1-\alpha_f}\right)\right]\mathbf{x}_{n+1} \\ &\quad + \alpha_f \mathbf{K}(\mathbf{x}_{n+1-\alpha_f})\mathbf{x}_n \\ &= \mathbf{Q}\left(t_{n+1-\alpha_f}\right) \\ &\quad + \mathbf{M}\left[\frac{1-\alpha_m}{\beta\Delta t^2}\mathbf{x}_n + \frac{1-\alpha_m}{\beta\Delta t}\dot{\mathbf{x}}_n + \frac{1-\alpha_m-2\beta}{2\beta}\ddot{\mathbf{x}}_n\right] \\ &\quad + \mathbf{C}\left[\frac{\left(1-\alpha_f\right)\gamma}{\beta\Delta t}\mathbf{x}_n + \frac{\left(1-2\alpha_f\right)\beta - \left(1-\alpha_f\right)\gamma}{\beta}\dot{\mathbf{x}}_n\right. \\ &\quad \left. - \Delta t\left(1-\alpha_f\right)\left(1-\frac{\gamma}{2\beta}\right)\ddot{\mathbf{x}}_n\right]. \end{aligned} \tag{24}$$

Equation (24) is a group of nonlinear algebraic equations and is solved by the Newton–Raphson method.

4 Examples and discussion

4.1 Code verification

Before applied to the case with periodic load, the proposed solution procedure and codes are applied first to the case with constant load for verification. If a constant load σ_0 is distributed uniformly over the membrane and the membrane deformation is very small, the static equilibrium shape [24] of the membrane is governed by

$$\frac{\mathrm{d}^2 z}{\mathrm{d}x^2} = -\frac{\sigma_0}{T}, \tag{25}$$

which has an exact solution as

$$z = \beta x\,(1-x)\,, \tag{26}$$

where

$$\begin{cases} \beta = \sigma_0/2T \\ T = Eh\left[\delta_0 + \left(\beta\sqrt{1+\beta^2} + sinh^{-1}\beta\right)/2\beta - 1\right] \end{cases} \tag{27}$$

Hence, this problem can be used to test the accuracy of the proposed finite element procedure and corresponding codes by simplifying Eq. (10) into

$$\rho_S h\frac{\partial^2 z}{\partial t^2} + \rho_S C_d\frac{\partial z}{\partial t} - T\frac{\partial^2 z}{\partial x^2} = \sigma_0 \tag{28}$$

Two cases with $\rho_S = 1000, h = 0.001, C_d = 0.001$, $\sigma = 1.0$, $E = 25{,}000$ and $\delta_0 = 0$ and $\delta_0 = 0.02$ are considered, and the corresponding values of parameter β in Eq. (27) are 0.449 and 0.415, respectively. In both cases, the membrane is divided into $M = 20$ elements and the time step is taken as $\Delta t = 0.005$. As shown in Fig. 3, the computed membrane deformations have an excellent agreement with the exact solutions.

4.2 Grid independence test

To test the influence of the grid density and make the numerical results more reliable, dynamic responses of the membrane with $\rho_S = 1000$, $h = 0.001$, $C_d = 0.001$, $\sigma = 1.0$, $f_e = 1.0$, $E = 25{,}000$, $\delta_0 = 0$, $\Delta t = 0.005$ and $t \in [0, 100]$ are computed first using four meshes with $M = 5$, 10, 20 and 40. In all cases, the initial conditions are defined as $z = 0$, $\dot{z} = 0$ and $\ddot{z} = 0$.

In Figs. 4 and 5, the computed time history of the displacement at the centre point of the membrane in time interval $t \in [95, 100]$ and the instantaneous membrane deformation at $t = 100$ are presented, respectively. As shown in the figures, with increase in the total number of the element, discrepancy between the results is decreased. In particular, the computed centre point displacement in Fig. 4 and the membrane deformation in Fig. 5 are changed very small when M is increased from 20 to 40. This means that a solution independent of the mesh size could be obtained at $M = 20$. Hence, $M = 20$ is used for all computations hereafter.

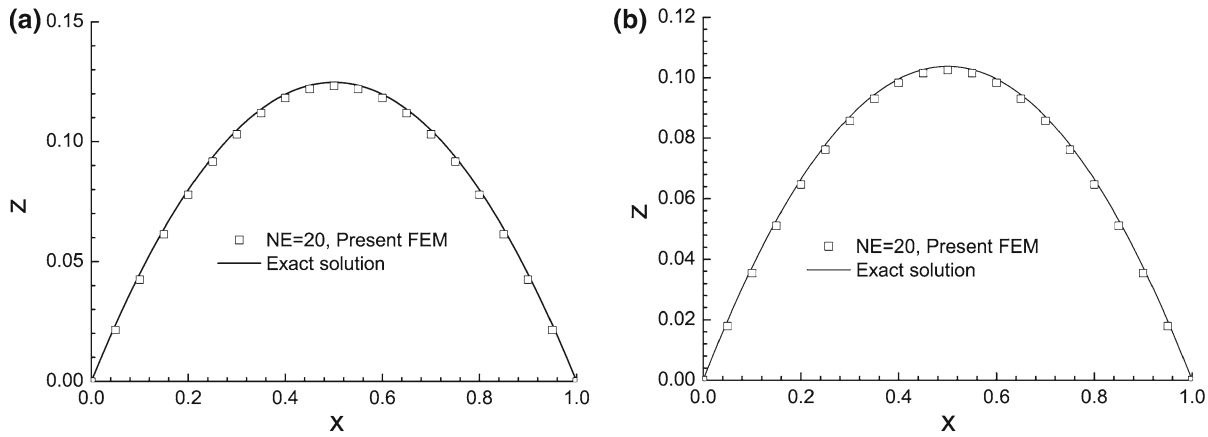

Fig. 3 Final deformations of the membrane under constant load. **a** $\delta_0 = 0$. **b** $\delta_0 = 0.02$

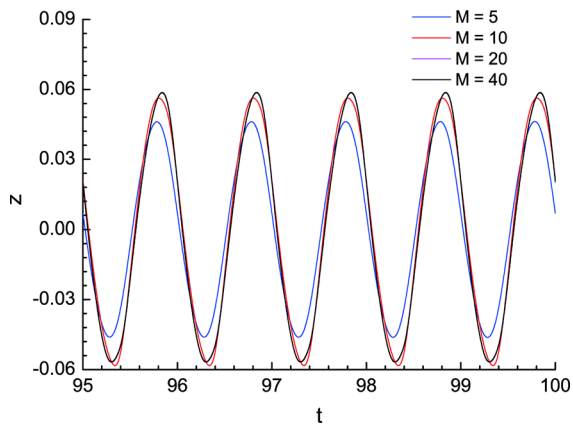

Fig. 4 Time histories of the displacement at the centre point of the membrane ($t = 95-100$)

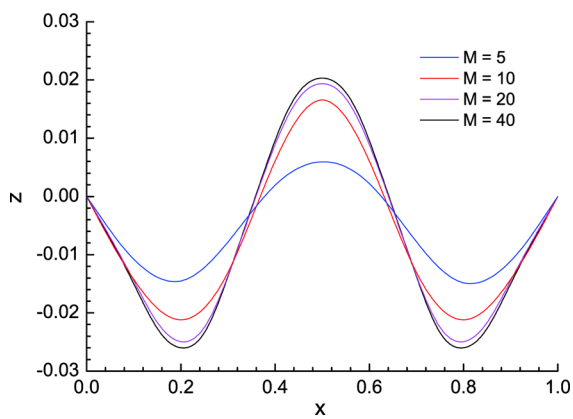

Fig. 5 Instantaneous deformation of the membrane at $t = 100$

In addition, in the following sections, when effect of one parameter is investigated, the values of other parameters will remain the same as this section.

4.3 Effect of density

To investigate the effect of the membrane density ρ_S, dynamic responses of a flexible membrane under periodic load when ρ_S is increased from 1 to 700 are simulated. In Fig. 6, instantaneous positions of the centre point in $t \in [80, 100]$ when its velocity becomes zero (or changes direction) are presented to illustrate the final state of the vibration state at the membrane centre. In fact, the points in Fig. 6 can also be taken as a Poincare map of the phase portraits by taking the plane $\dot{z} = v = 0$ as the Poincare section.

As shown in Fig. 6, when the non-dimensional density ρ_S is decreased from 700 to 1, vibration state of membrane centre will change greatly. As marked in Fig. 6a, the bifurcation diagram with respect to ρ_S can be divided roughly into four regions:

Region I ($\rho_S \in [549.5, 700]$) As shown in Figs. 6a and 7, in this region the vibration of the membrane centre is always period 1 and has the same period with the external load, namely $T_c = T_e = 1.0$. With decrease in ρ_S, the amplitude of vibration is increased continuously.

Region II ($\rho_S \in [125.5, 549.5]$) As shown in Figs. 6a and 8, vibration state in this region is also period 1 with $T_c = T_e = 1.0$. However, different from region I, the amplitude of vibration in this region is much larger and decreased with ρ_S, and the two branches in the bifur-

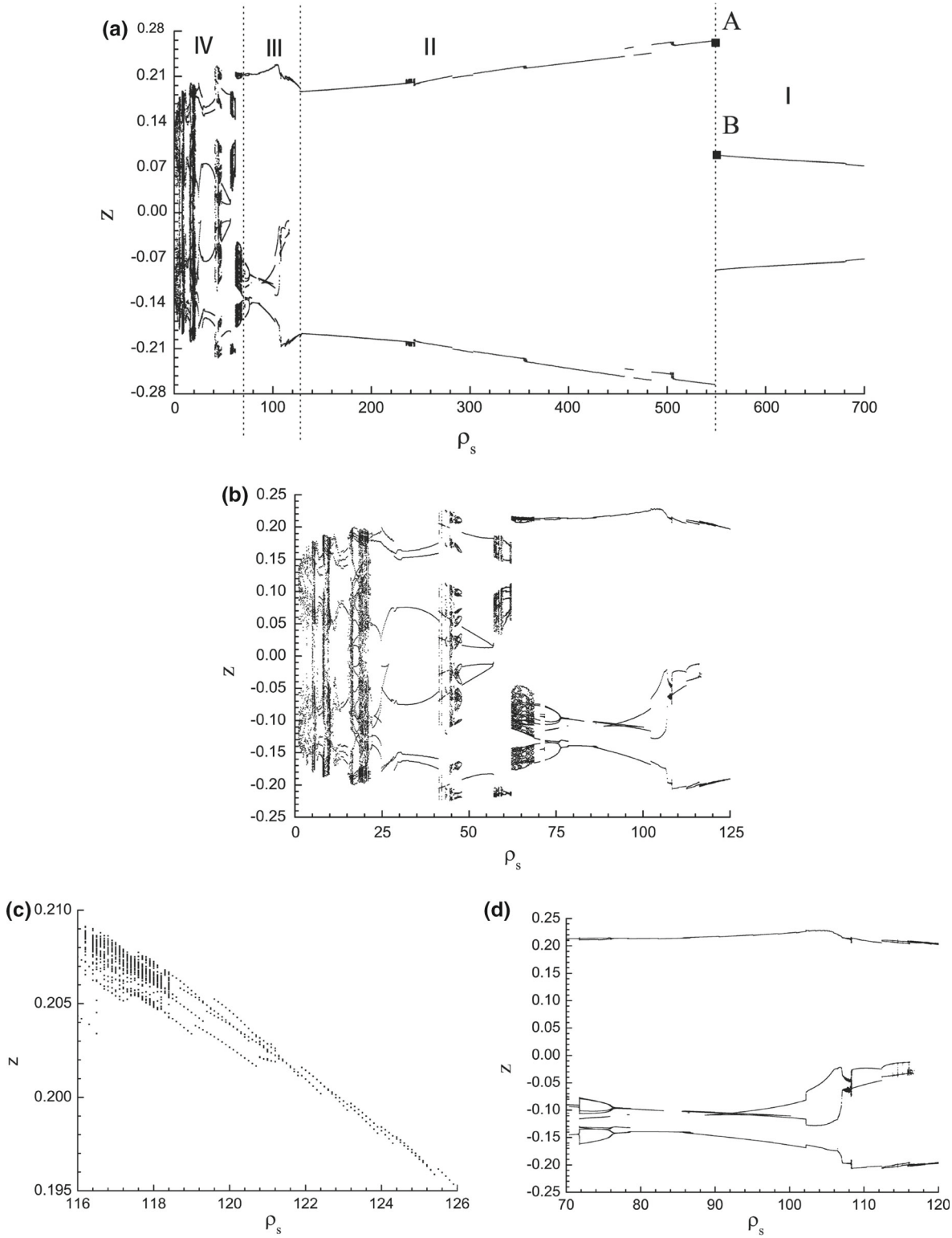

Fig. 6 Bifurcation diagram at the centre point of the membrane with respect to ρ_S. **a** $\rho_S \in [0, 700]$. **b** $\rho_S \in [1, 125]$. **c** $\rho_S \in [116, 126]$ (upper branch). **d** $\rho_S \in [70, 120]$

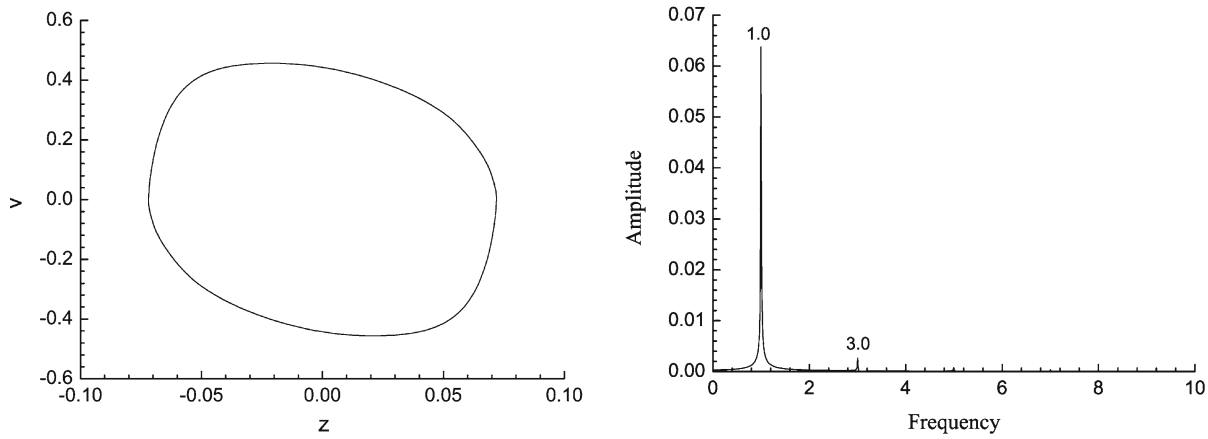

Fig. 7 Phase portrait and spectrogram at $\rho_S = 700$

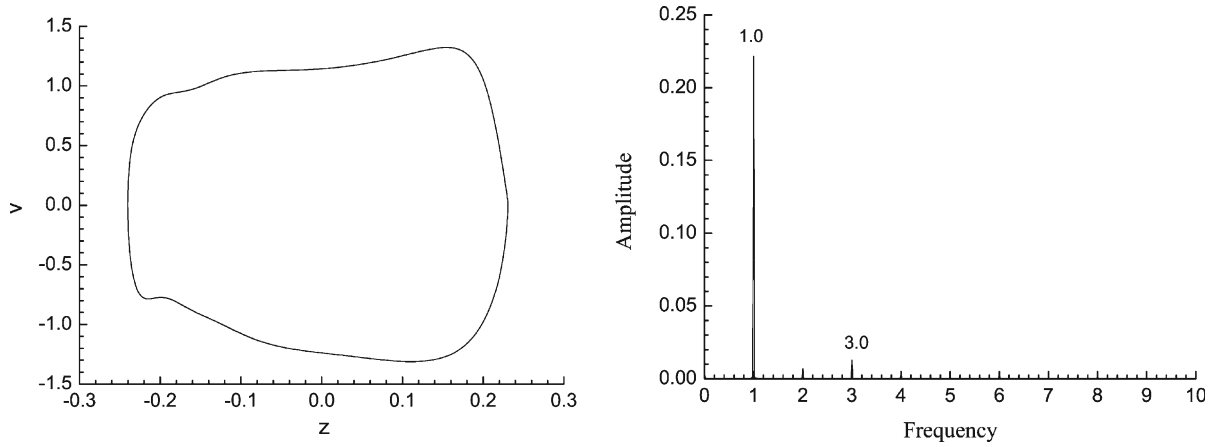

Fig. 8 Phase portrait and spectrogram at $\rho_S = 400$

cation diagram have become discontinuous at several points. Moreover, the amplitude of the harmonic component with $f_c = 3$ is increased in Fig. 8.

On the boundary between regions I and II in Fig. 6a, the amplitude of the membrane centre is increased abruptly from 0.0887 to 0.265 when ρ_S is decreased slightly near $\rho_S = 549.5$. To study the reason for this phenomenon, dynamic responses of the membrane from 40 different initial velocities (see the red points in Fig. 9) are computed at both $\rho_S = 548.4$ (point A in Fig. 6a) and 549.5 (point B in Fig. 6a). As shown in Fig. 9, in both cases two stable orbits (i.e. the limit cycle oscillation, LCO) can be observed in the phase plane, and the trajectories initiated from some of the initial points are eventually attracted by LCO1 while the others are attracted by LCO2. In Fig. 9, the trajectory initiated from $z = 0$ and $v = 0$ is also presented and highlighted by blue colour. As seen, the trajectory from $z = 0$ and $v = 0$ is eventually attracted by LCO1 at $\rho_S = 548.4$ while by LCO2 at $\rho_S = 549.5$. Hence, because the amplitude of LCO1 is much larger than LCO2, an abrupt jump between point A and point B is observed in Fig. 6a.

Region III ($\rho_S \in [68.6, 125.5)$) As shown in Fig. 6, various types of periodic vibration can be observed in this region. First, when ρ_S is decreased in $\rho_S \in [116.8, 125.5)$, it can be seen from Fig. 6c that the period of vibration at the membrane centre is increased gradually from T_e to $2T_e$ in $\rho_S \in [121.5, 125.5)$, $4T_e$ in $\rho_S \in [118.5, 121.5)$ and other periodic vibrations with higher periods in $\rho_S \in [116.8, 118.5)$, which can be seen more clearly from the phase portraits and

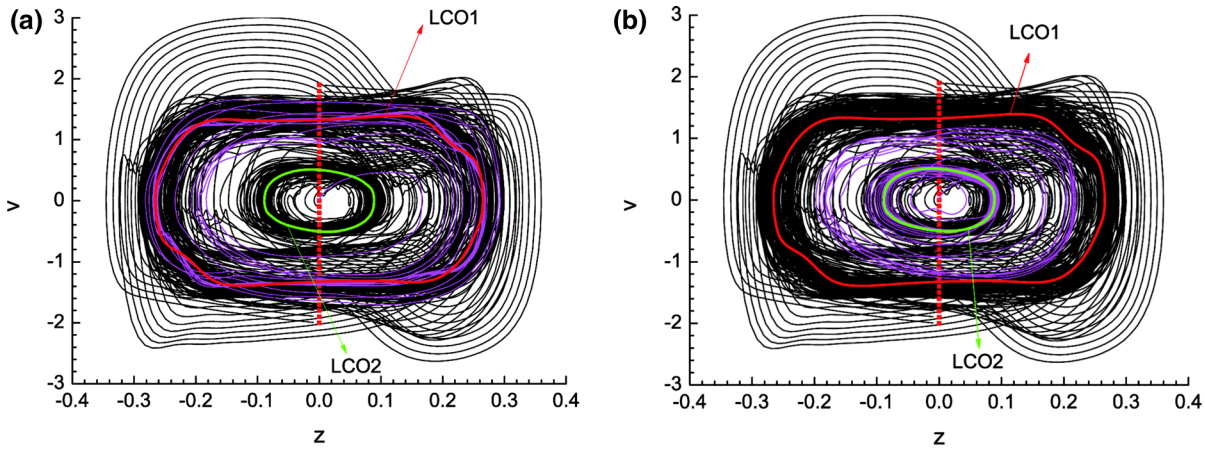

Fig. 9 Phase portraits from different initial points. **a** $\rho_S = 548.4$ (point A). **b** $\rho_S = 549.5$ (point B)

spectrograms given in Fig. 10. As shown in the figures, the membrane is still vibrating near LCO1 in $\rho_S \in [116.8, 125.5)$ with more harmonic components than region II. Moreover, although the vibration states at $\rho_S = 122$, 120 and 117 are very different, the amplitudes of their dominant vibration components are not changed very much.

Then, when ρ_S is decreased in $\rho_S \in [68.6, 116.8)$, it can be seen from Figs. 6d and 11 that dynamic responses of the membrane centre are still periodic and the period is also increased with ρ_S. However, different from the vibration state in $\rho_S \in [116.8, 125.5)$, two new branches appear in Fig. 6d when ρ_S is less than 116.8, which can also be seen from the phase portraits. As shown in Fig. 11, different from those in Fig. 10, the trajectories at $\rho_S = 73, 93$ and 110 are twining not only around LCO1 but also LCO2. Moreover, it can also be found from the spectrograms in Fig. 11 that the number of the dominant frequency components has increased in $\rho_S \in [68.6, 116.8)$ compared with $\rho_S \in [68.6, 125.5)$. *Region IV* ($\rho_S \in [1, 68.6)$) As shown in Fig. 6, when ρ_S is decreased near 68.6, the vibration state at the membrane centre will become very complicated. As shown in Fig. 6b, this region can be further divided into several subregions, such as $\rho_S \in [62.5, 68.6)$, $[57.1, 58.6]$, $[18.3, 21.3]$ and $[8, 10]$, connected by several periodic windows.

In Fig. 12, the phase portraits and spectrograms at $\rho_S = 68$, 50, 45, 30 and 20 are given. As shown in Fig. 12a, quite different from those in Figs. 7, 8, 10 and 11, the vibration has become quasi-periodic at $\rho_S = 68$ and two irrational frequency peaks are observed near 2.45 and 4.53. Then, the number of irrational frequency components is increased in Fig. 12c when ρ_S is decreased to 45, and finally the spectrogram becomes almost continuous in Fig. 12e at a much smaller density of $\rho_S = 20$, which may indicate the vibration has turn to chaotic. Moreover, it can be seen from Fig. 12b, d that the vibration periods in both of the windows $\rho_S \in [47, 57.1]$ and $\rho_S \in [27, 44]$ are $3T_e$. This could be another proof of the appearance of chaotic vibration according to the Li–Yorke conjecture of "Period three implies chaos"[25].

Finally, the change of vibration state of the membrane centre with respect to ρ_S is summarized in Table 1. As shown in the table, with decrease in ρ_S, the vibration state at the membrane centre has varied from period 1 to period 2, period 4, multi-period with higher period, quasi-period and chaos. These results have shown that the mass/inertia of the membrane, which is usually ignored in many previous studies of FMI, has very great effect on the dynamic response of the membrane wing under unsteady fluid loads. In addition, it seems that increasing the mass/inertia of the membrane could make its response under periodic fluid loads more regular and controllable.

4.4 Effect of elastic modulus

The effect of the non-dimensional elastic modulus E on the dynamic response of the membrane is considered by changing it from 100 to 100,000, and Fig. 13 presents the bifurcation diagram of the vibration at the mem-

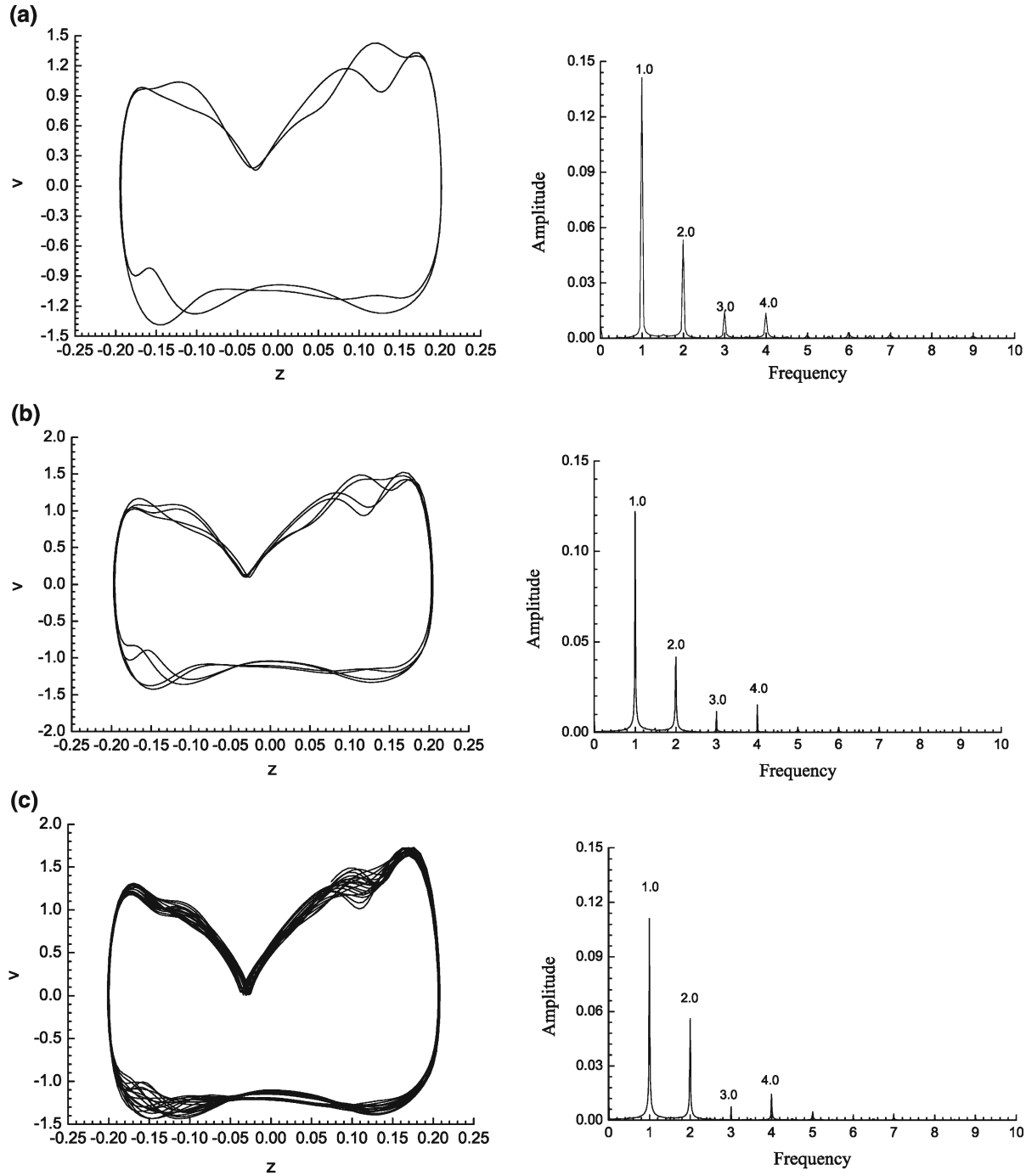

Fig. 10 Phase portrait and spectrogram at several membrane densities in $\rho_S \in [116.8, 125.5)$. **a** $\rho_S = 122(T_c = 2T_e)$. **b** $\rho_S = 120(T_c = 4T_e)$. **c** $\rho_S = 117(T_c = 18T_e)$

brane centre with respect to E. As shown in Fig. 13a, the bifurcation diagram in $E \in [100, 100{,}000]$ can be divided roughly into three regions.

Region I ($E \in [100, 1182.9]$) As shown in Figs. 13a and 14, in this region the final state of vibration at the membrane centre is period 1 with $T_c = T_e$, and

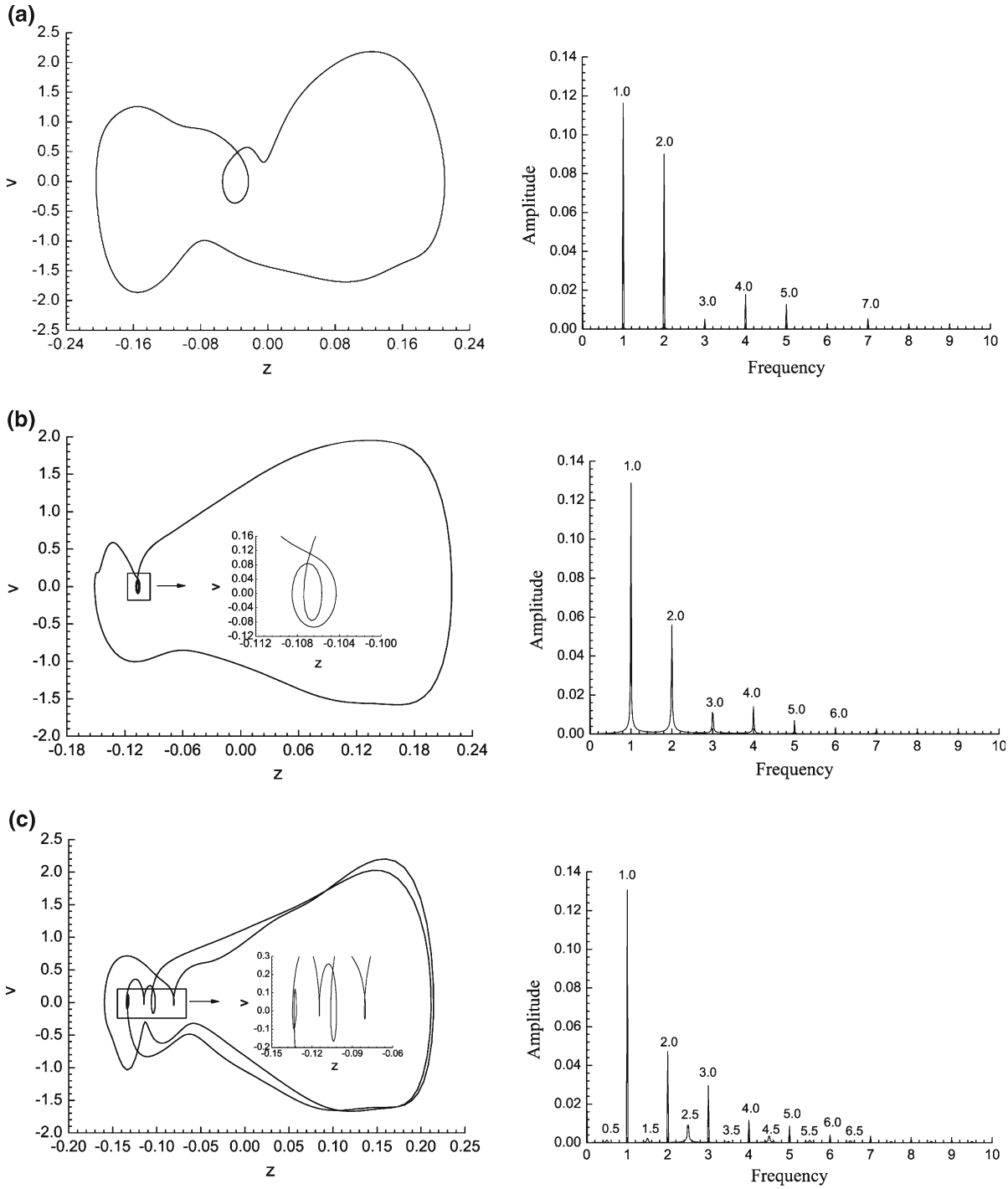

Fig. 11 Phase portrait and spectrogram at several membrane densities in $\rho_S \in [68.6, 116.8)$. **a** $\rho_S = 110(T_c = 2T_e)$. **b** $\rho_S = 93(T_c = 3T_e)$. **c** $\rho_S = 73(T_c = 6T_e)$

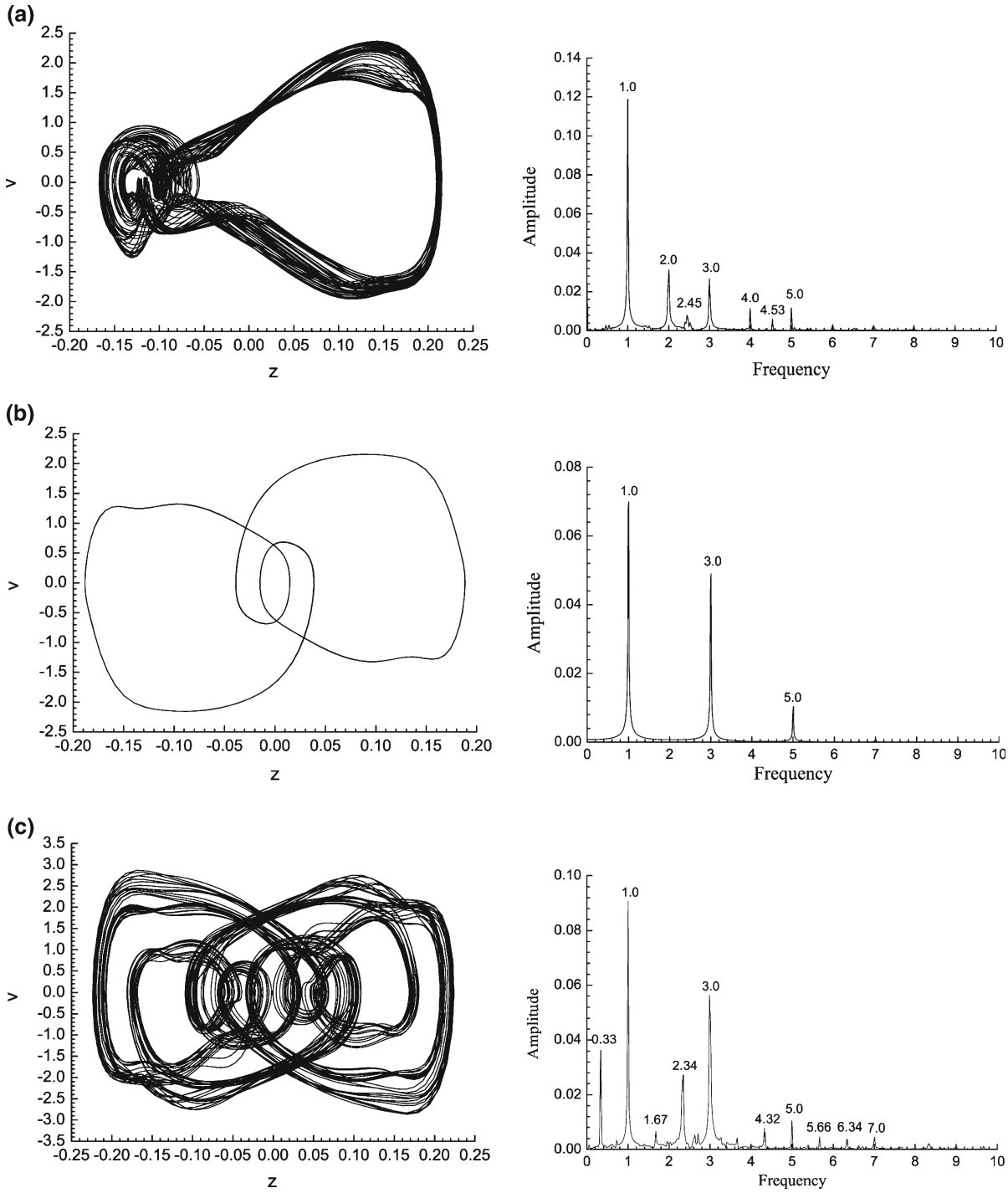

Fig. 12 Phase portrait and spectrogram at several membrane densities in $\rho_S \in (0, 68.6)$. **a** $\rho_S = 68$. **b** $\rho_S = 50$. **c** $\rho_S = 45$. **d** $\rho_S = 30$. **e** $\rho_S = 20$

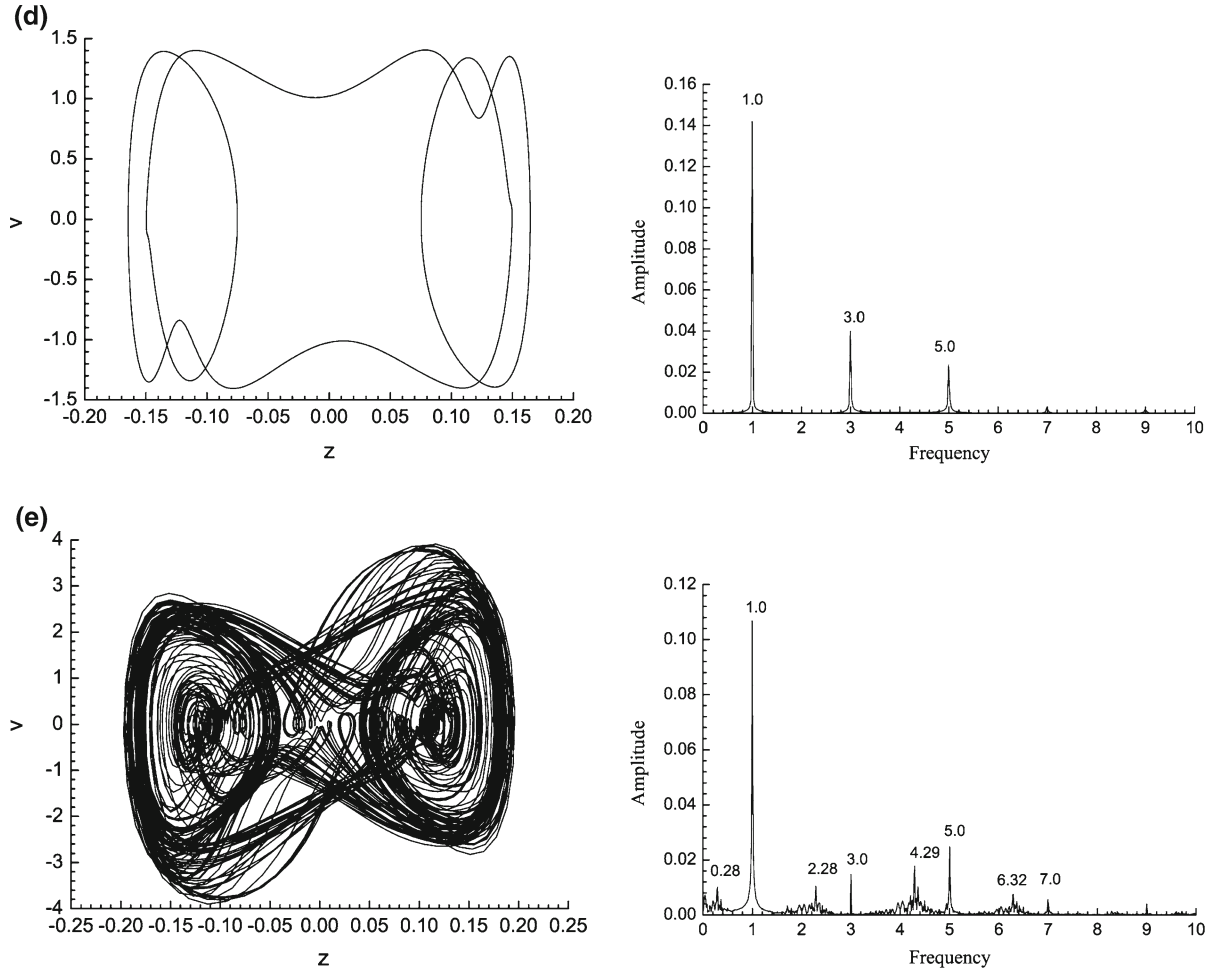

Fig. 12 continued

Table 1 Variation of the vibration state with respect to the membrane density

Region	I	II	III	IV
Range of ρ_S	[549.5, 700]	[125.5, 549.5)	[68.6, 125.5)	[1, 68.6)
Vibration state	Period 1	Period 1	Period 2, period 4 and other multi-period with higher period	Quasi-period and chaos with period-3 windows

the amplitude of vibration is increased gradually with E in a wave form. At each wave crest or trough, the bifurcation curves will become discontinuous and jump abruptly from one branch to another with different characteristics, as shown in Fig. 13a. In Section 4.3, similar phenomenon of jump in the bifurcation diagram has been discussed and it is found caused by the jump of the vibration state between two stable orbits. To examine whether the jump in Fig. 13 caused by the same reason as that in Fig. 6, dynamic responses at $E = 663.5$ (point A Fig. 13a) and $E = 668.4$ (point B in Fig. 13a) initiated from 40 different initial states are simulated and the obtained phase portraits are shown in Fig. 15. As shown in Fig. 15a, at $E = 663.5$ trajectories from all initial conditions are attracted eventually by a stable periodic orbit (LCO1) after a transient process.

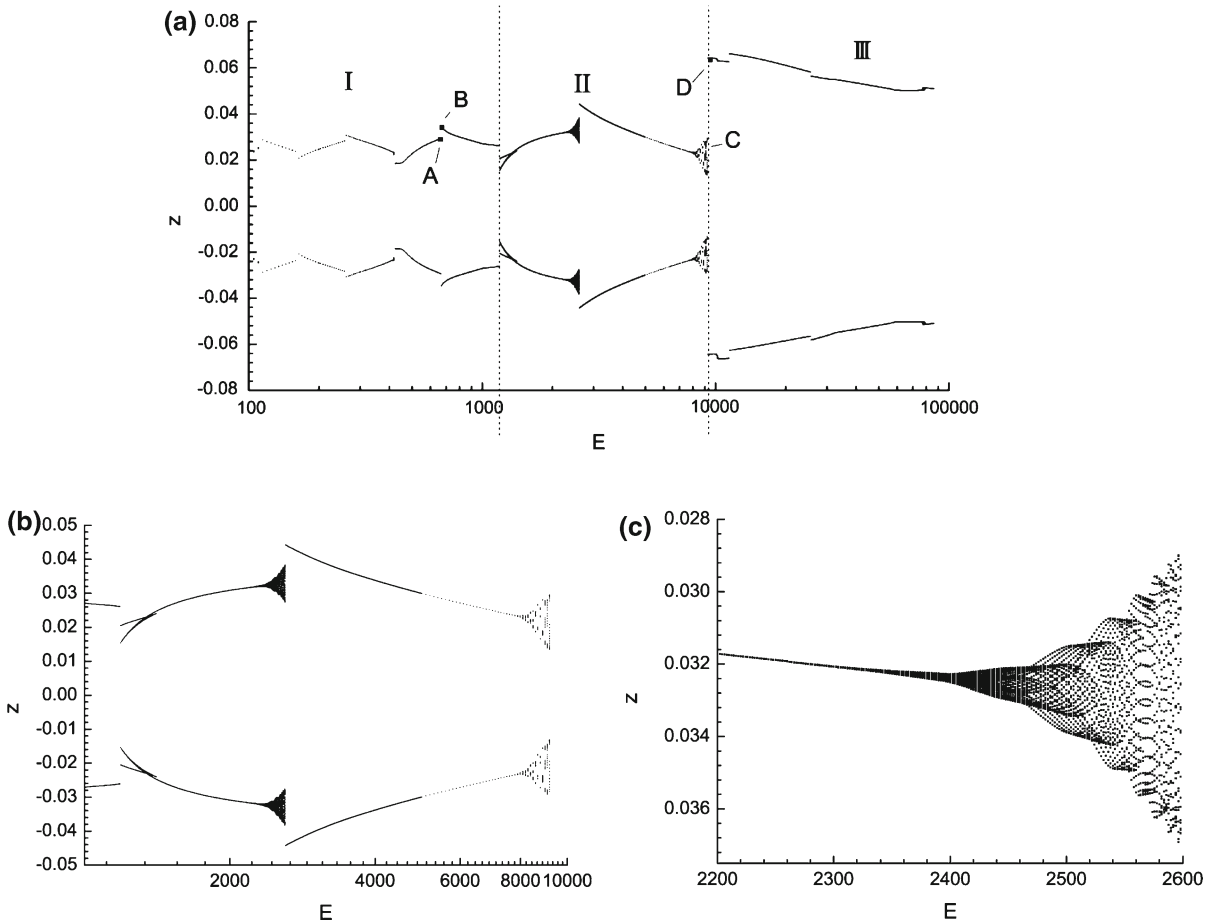

Fig. 13 Bifurcation diagram with respect to E. **a** $E \in [100, 100{,}000]$. **b** $E \in [1000, 10{,}000]$. **c** $E \in [2200, 2600]$ (upper branch)

At $E = 668.4$, however, another stable periodic orbit (LCO2) is observed and the trajectories from some initial conditions are eventually attracted by LCO1 while the others attracted by LCO2. In particular, the trajectory from $z = 0$ and $v = 0$ is attracted by LCO1 at $E = 663.5$ while by LCO2 at $E = 668.4$. Hence, a jump is observed in Fig. 13a when E is increased very slightly from 663.5 to 668.4, which indicates that the reason of the jumps in Figs. 6 and 13 are very similar. However, because the difference of the amplitude between LCO1 and LCO2 in Fig. 15 is much smaller than that in Fig. 9, the jump between A and B in Fig. 13a is not as significant as that in Fig. 6a.

Region II ($E \in (1182.9, 9190.9]$) As shown in Fig. 13b, in this region the vibration amplitude is also increased gradually with E in a wave form, but the vibration state has become more complicated. As shown in the figure, near the boundary of region I and region II, the vibration jumps from LCO2 to LCO1. However, different from that in region I, the period of LCO1 is $T_c = 3T_e$ near $E = 1182.9$ and then turn back to $T_c = T_e$ when $E \in [1480.3, 2200]$, as shown in Figs. 13b and 16a. When E is further increased, the stability of LCO1 is decreased and the vibration changes gradually from periodic to quasi-periodic in $E \in [2200, 2600]$, as shown in Figs. 13c and 16(b). Then, near $E = 2600$, the vibration state will jump from LCO1 back to LCO2. With further increase in E, the stability of LCO2 will also be decreased when $E \in [7392, 9190.9]$.

Region III ($E \in (9190.9, 100{,}000]$) As shown in Fig. 13a, near $E = 9190.9$ the vibration state will jump from quasi-period to period 1 when E is increased slightly. In Fig. 17, trajectories from 40 different initial points at $E = 9190.9$ (point C in Fig. 13a) and $E = 9290.8$ (point D in Fig. 13a) are given to illustrate

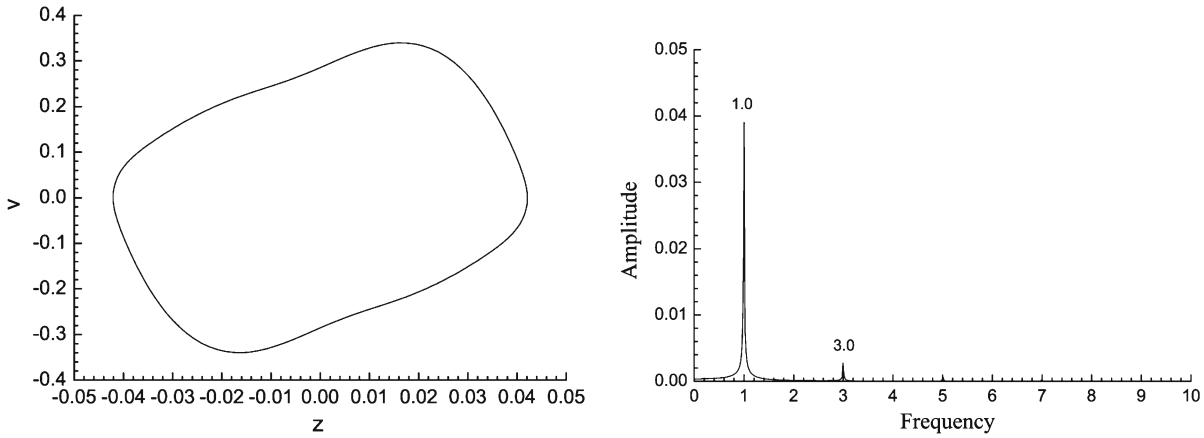

Fig. 14 Phases portrait and spectrogram at $E = 1100$

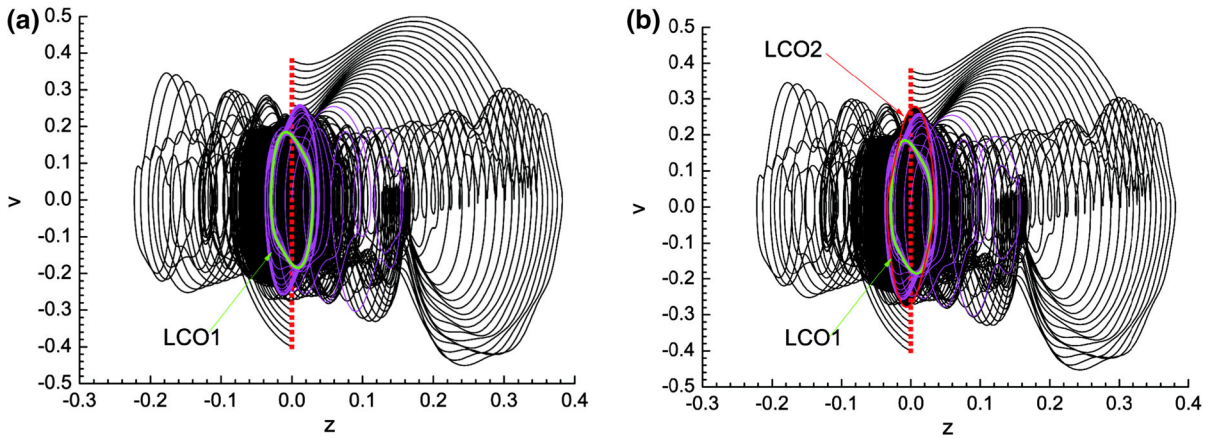

Fig. 15 Phase portraits from different initial points at $E = 663.5$ and $E = 668.4$. **a** $E = 663.5$ (point A). **b** $E = 668.4$ (point B)

more clearly the change in the vibration state here. As seen, at both $E = 9190.9$ and $E = 9290.8$, LCO2 has become quasi-periodic and another stable periodic orbit (LCO3) with larger amplitude appears in the phase plane. Because the trajectory initiated from $z = 0$ and $v = 0$ is attracted by LCO2 at $E = 9190.9$ while by LCO3 at $E = 9290.8$, the amplitude in the bifurcation diagram is jumped from point C to D in Fig. 13a. Then, when E is increased from 9290.9 to 100,000, the vibration state of the membrane centre is no longer changed very much expect that the amplitude of LCO3 is decreased gradually.

4.5 Effect of pre-strain

With other parameters fixed, the effect of pre-strain on the dynamic response of the membrane under periodic load is investigated by increasing δ_0 from 0 to 0.08. As shown in the bifurcation diagram in Fig. 18 and the phase portrait and spectrogram in Fig. 19, the amplitude of the vibration is first decreased and then increased with δ_0, but the vibration state is always period 1 with $T_c = T_e$. Compared with the density and elastic modulus, the pre-strain has smaller influence on the dynamic response of the membrane.

4.6 Vibration along the membrane

In the above sections, only the dynamic response at the centre point of the membrane is considered. In fact, in most of the existing FMI studies, the centre point is also taken as the indicator of the vibration state of the whole membrane. Can the centre point reflect correctly the

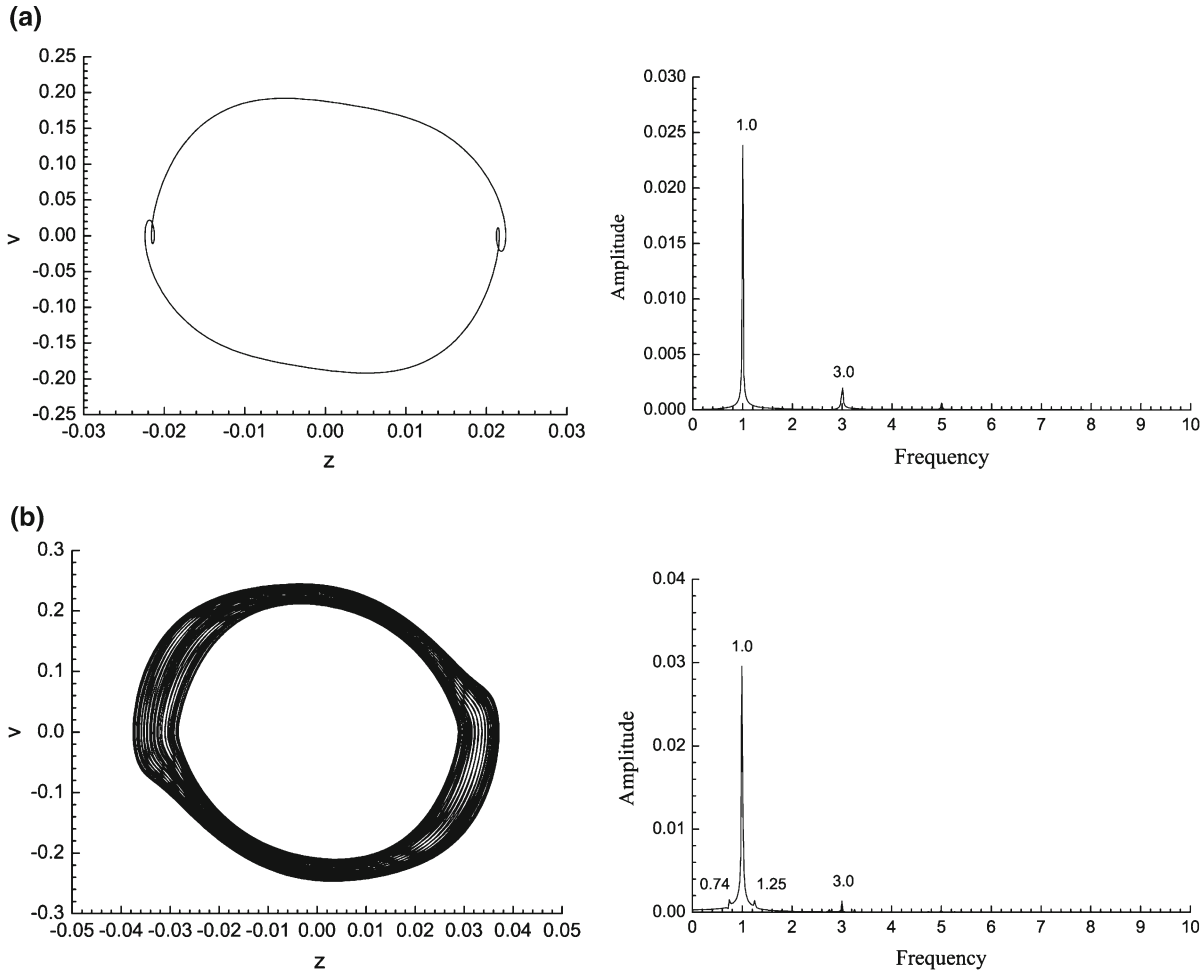

Fig. 16 Phases portraits and spectrogram at several E. **a** $E = 1300$. **b** $E = 2600$

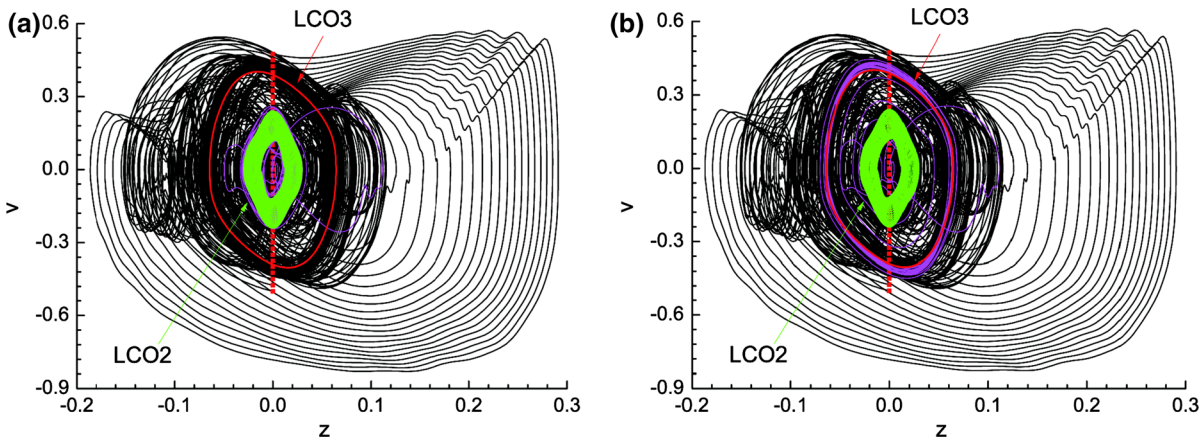

Fig. 17 Phase portraits from different initial points at $E = 9190.9$ and $E = 9290.8$. **a** $E = 9190.9$. **b** $E = 9290.8$

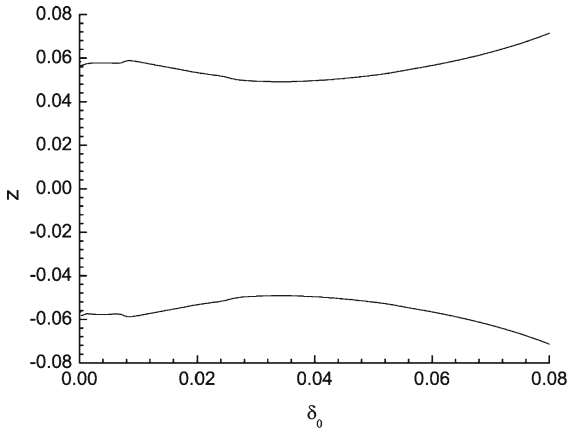

Fig. 18 Bifurcation diagram with respect to δ_0

vibration state of the whole structure? In this section, this is investigated based on the results of Section 4.3.

In Fig. 20, bifurcation diagrams with respect to x are given to illustrate the vibration states of the whole membrane at several membrane densities. As seen, at $\rho_S = 300$ (Fig. 20a),$\rho_S = 50$ (Fig. 20d) and $\rho_S = 20$ (Fig. 20f), the vibration states at different membrane points are very similar. Taking $\rho_S = 50$ in Fig. 20d as an example, although the amplitude is decreased from the centre point ($x = 0.5$) to the two ends ($x = 0$ and $x = 1$), the vibration states at almost all locations are period 3. In this case, the vibration states at other membrane points can be reflected by the centre point. However, at $\rho_S = 120$ (Fig. 20b), $\rho_S = 70$ (Fig. 20c) and $\rho_S = 30$ (Fig. 20e), the situation is quite different and the vibration state will change greatly along the membrane. Taking $\rho_S = 30$ in Fig. 20e as an example, the vibration of the membrane is period 3 in $x \in (0, 0.15]$, $x \in [0.33, 0.66]$ and $x \in [0.85, 1)$ but becomes period 2 in $x \in (0.15, 0.33)$ and $x \in (0.66, 0.85)$, which means the vibration state at other positions might different from that at the membrane centre point. In this case, the vibration state of the whole membrane cannot be reflected correctly if only taking the membrane centre as the indicator.

5 Conclusions

Nonlinear vibrations of a flexible membrane under external periodic loads is computed using the standard finite element method and Generalized-α method, and the effects of the membrane density, elastic modulus, pre-strain and location are investigated in detail. From the obtained numerical results, several conclusions could be made as follows:

(1) Using the standard finite element method for spatial discretization, Generalized-α method for temporal integration and Newton–Raphson method for the nonlinear algebra equations, an accurate and robust numerical scheme can be obtained for the nonlinear vibration of a flexible membrane under time-varying loads. With little modification, the solution procedure proposed here can be employed as the structure solver for FMI simulations.

(2) With decrease in the membrane density, vibration state of the membrane is varied gradually from period 1 to multi-period, quasi-period and chaos

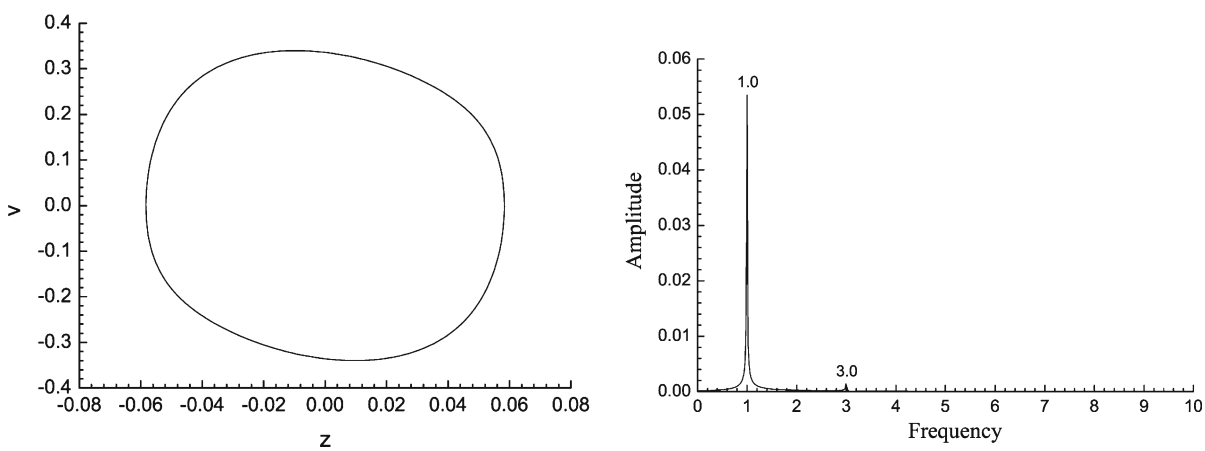

Fig. 19 Phases portrait and spectrogram at $\delta_0 = 0.01$

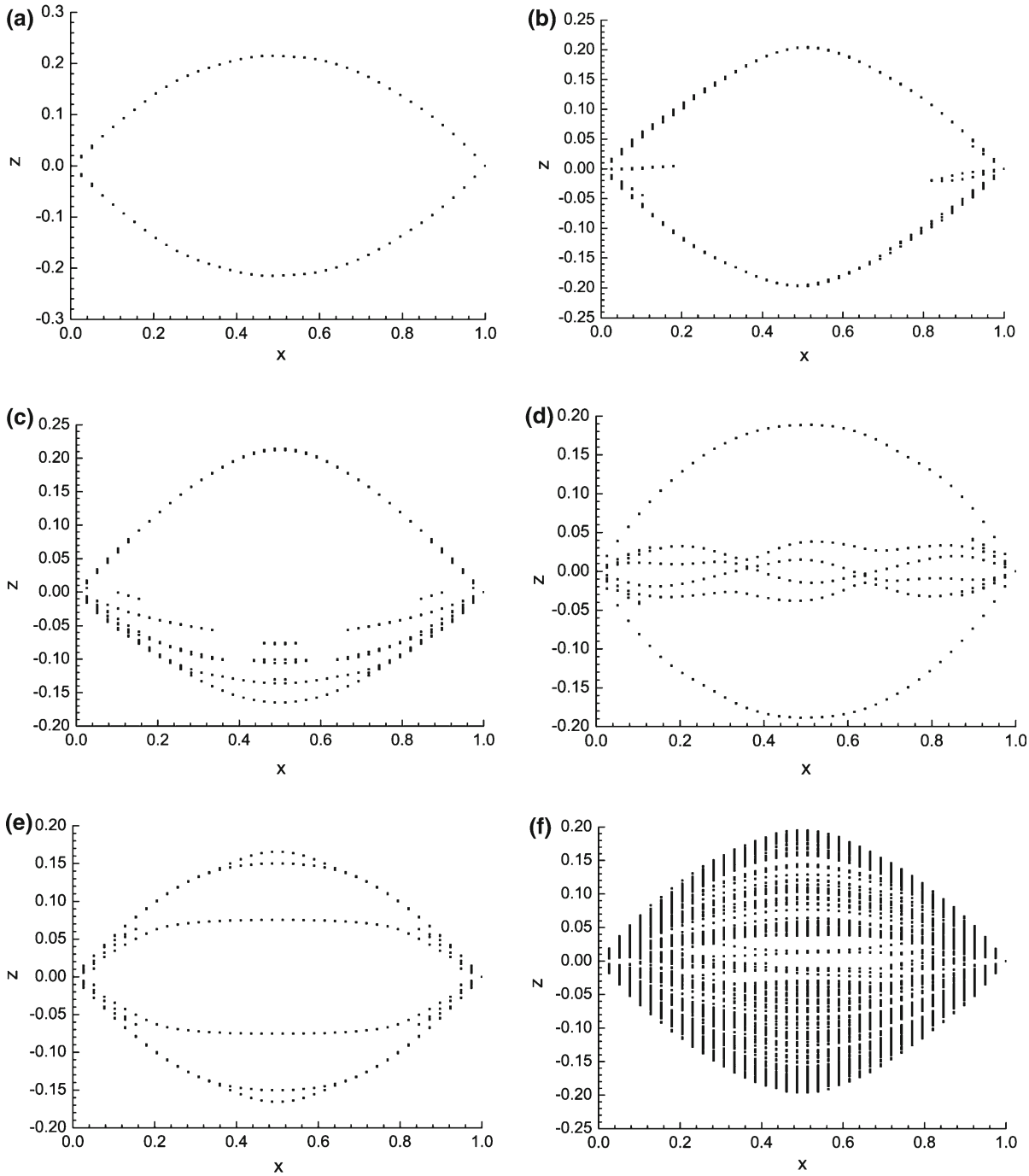

Fig. 20 Bifurcation diagram with respect to x at several membrane densities. **a** $\rho_S = 300$. **b** $\rho_S = 120$. **c** $\rho_S = 70$. **d** $\rho_S = 50$. **e** $\rho_S = 30$. **f** $\rho_S = 20$

although the external load is uniform and periodic. This indicates that the mass/inertia, which is usually ignored in the existing FMI analysis, has great influence on the dynamic response of the flexile membrane when unsteady fluid loads are imposed, and FIV of the membrane structures with larger mass/inertia is more regular and controllable.

(3) For a flexible membrane under periodic loads, the vibration state might change suddenly at some membrane densities and elastic moduli. Near these critical structure parameters, it is found that there is more than one stable orbit in the phase portraits and the final state of vibration will jump between them.
(4) Compared with the density and elastic modulus, the effect of pre-strain on the dynamic response of the membrane is much smaller.
(5) At some structure parameters, the computed vibration states of the centre point are quite different with those at other membrane locations. It means that, for membrane and other continuous structures, taking the centre point as the indicator of the vibration state of the whole structure might lead to mistakes in some cases. For the vibration problems involving continuous structures such as membrane, beam and rod, new methods or indicators should be developed to reflect more accurately the vibration state of the whole structure.

Acknowledgments This work is supported by Science Foundation of China University of Petroleum, Beijing (No. 2462014YJRC007), National Natural Science Foundation of China (No. 51506224) and National Key Basic Research Program of China (973 Program, No. 2012CB026002). The author would like to thank for the kindly support of these foundations.

References

1. de Matteis, G., de Socio, L.: Nonlinear aerodynamics of a two-dimensional membrane airfoil with separation. J. Aircr. **23**(11), 831–836 (1986)
2. Rast, M.P.: Simultaneous solution of the Navier–Stokes and elastic membrane equations by a finite element method. Int. J. Numer. Methods Fluids **19**, 1115–1135 (1994)
3. Smith, R., Shyy, W.: Computation of unsteady laminar flow over a flexible two-dimensional membrane wing. Phys. Fluids **7**, 2175 (1995)
4. Smith, R., Shyy, W.: Computation of aerodynamic coefficients for a flexible membrane airfoil in turbulent flow: a comparison with classical theory. Phys. Fluids **8**, 3346 (1996)
5. Ling, S.-J., Neitzel, G.P., Aidun, C.K.: Finite element computations for unsteady fluid and elastic membrane interaction problems. Int. J. Numer. Methods Fluids **24**, 1091–1110 (1997)
6. Matthews, L.A., Greaves, D.M., Williams, C.J.K.: Numerical simulation of viscous flow interaction with an elastic membrane. Int. J. Numer. Methods Fluids **57**, 1577–1602 (2008)
7. Rojratsirikul, P., Wang, Z., Gursul, I.: Unsteady fluid–structure interactions of membrane airfoils at low Reynolds numbers. Exp. Fluids **46**(5), 859–872 (2009)
8. Rojratsirikul, P., Wang, Z., Gursul, I.: Effect of pre-strain and excess length on unsteady fluid–structure interactions of membrane airfoils. J. Fluids Struct. **26**(3), 359–376 (2010)
9. Rojratsirikul, P., Genc, M., Wang, Z., Gursul, I.: Flow-induced vibrations of low aspect ratio rectangular membrane wings. J. Fluids Struct. **27**, 1296–1309 (2011)
10. Gordnier, R.E.: High-fidelity computational simulation of a membrane wing airfoil. J. Fluids Struct. **25**, 897–917 (2009)
11. Visbal, M.R., Gordnier, R.E., Galbraith, M.C.: High-fidelity simulations of moving and flexible airfoils at low Reynolds numbers. Exp. Fluids **46**, 903–922 (2009)
12. Gordnier, R.E., Attar, P.J.: Impact of flexibility on the aerodynamics of an aspect ratio two membrane wing. J. Fluids Struct. **45**, 138–152 (2014)
13. Jaworski, J.W., Gordnier, R.E.: High-order simulations of low Reynolds number membrane airfoils under prescribed motion. J. Fluids Struct. **31**, 49–66 (2012)
14. Jaworski, J.W., Gordnier, R.E.: Thrust augmentation of flapping airfoils in low Reynolds number flow using a flexible membrane. J. Fluids Struct. **52**, 199–209 (2015)
15. Visbal, M., Yilmaz, T.O., Rockwell, D.: Three-dimensional vortex formation on a heaving low-aspect-ratio wing: computations and experiments. J. Fluids Struct. **38**, 58–76 (2013)
16. Tregidgo, L., Wang, Z., Gursul, I.: Unsteady fluid–structure interactions of a pitching membrane wing. Aerosp. Sci. Technol. **28**, 79–90 (2013)
17. Arbós-Torrent, S., Ganapathisubramani, B., Palacios, R.: Leading- and trailing-edge effects on the aeromechanics of membrane aerofoils. J. Fluids Struct. **38**, 107–126 (2013)
18. Curet, O.M., Carrere, A., Waldman, R., Breuer, K.S.: Aerodynamic characterization of a wing membrane with variable compliance. AIAA J. **52**(8), 1749–1756 (2014)
19. Serrano-Galiano, S., Sandberg, R.D.: Direct numerical simulations of membrane wings at low Reynolds number. AIAA Paper 2015-1300 (2015)
20. Bleischwitz, R., de Kat, R., Ganapathisubramani, B.: Aspect-ratio effects on aeromechanics of membrane wings at moderate Reynolds numbers. AIAA J. **53**(3), 780–788 (2015)
21. Bleischwitz, R., de Kat, R., Ganapathisubramani, B.: Aeromechanics of membrane and rigid wings in and out of ground-effect at moderate Reynolds numbers. J. Fluids Struct. **62**, 318–331 (2016)
22. Waldman, R.M., Breuer. K.S.: Shape, lift, and vibrations of highly compliant membrane wings. AIAA Paper 2013-3177 (2013)
23. Chung, J., Hulbert, G.: A time integration algorithm for structural dynamics with improved numerical dissipation: the generalized-α method. J. Appl. Mech. **60**(2), 371–375 (1993)
24. Molki, M., Breuer, K.: Oscillatory motions of a prestrained compliant membrane caused by fluid–membrane interaction. J. Fluids Struct. **26**, 339–358 (2010)
25. Li, T.Y., Yorke, J.A.: Period three implies chaos. Am. Math. Mon. **82**, 985–992 (1975)